



## 17 **Abstract**

18 Earthquake migration patterns are important to reveal various triggering mechanisms, including  
19 the tectonic process and those caused by anthropogenic activities. Mapping out the spatial-  
20 temporal seismicity pattern is traditionally conducted using reference marks either in spatial or  
21 time. However, such mapping is particularly challenging for induced earthquakes because most  
22 industrial records that provide reference marks are unavailable to the public. Moreover, advances  
23 in earthquake detection techniques proliferate earthquake catalogs and thus require labor-  
24 intensive investigation. Therefore, a new methodology is demanded to automatically investigate  
25 spatial-temporal patterns of seismicity without reference marks. Here, we present a deep  
26 learning-based method to automatically identify the timings and locations of anomalous  
27 seismicity, defined by the sudden change of earthquakes in a region. We first rasterize multi-  
28 dimensional earthquake catalogs into 2-D distribution maps. Then, we identify the maps with  
29 anomalous seismicities and extract their timings and locations to generate condensed catalogs to  
30 reduce the manual effort in further investigation. We choose Changning and Weiyuan in Sichuan  
31 Basin as our study areas due to their high seismicity rates in recent years. We use the Changning  
32 catalog to train the method and the Weiyuan catalog to test the method's spatial transferability.  
33 Our approach successfully condenses both the Changning and Weiyuan catalogs with the  
34 accuracy of 0.87 based on the F1 score. The anomalous seismicities identified by our network  
35 include both earthquakes associated with hydraulic fracturing and aftershocks following strong  
36 quakes. As such, our method could be applied to broader areas with more complex migration  
37 patterns, including natural earthquake sequences.

## 38 **Plain Language Summary**

39 Earthquakes migrate in space and time, sometimes forming clusters due to various mechanisms.  
40 Detecting anomalies in seismicity patterns helps understand why they occur and can play critical  
41 roles in seismic hazard mitigation. Although finding anomalies in a single dimension is  
42 straightforward, it is challenging to detect anomalies in earthquake patterns when spatial and  
43 temporal information is coupled together. A prior information either in space or time is normally  
44 required to analyze seismicity, but such information is not always available for induced  
45 earthquakes. Therefore, a new method is required to decouple the spatial and temporal  
46 information, providing references in at least one domain without prior knowledge. Here, we  
47 develop a deep-learning-based method to identify timings of abnormal seismicity. With these  
48 timings as references, the anomalies in the spatial domain will be apparent and can be easily  
49 extracted. With our method, the investigation of induced earthquakes will no longer depend on  
50 prior knowledge from industrial records.

## 51 **1 Introduction**

52 Earthquakes evolve spatially over time, and some patterns of the evolution provide  
53 important insights into the mechanisms driving earthquakes and their interactions (Freed, 2005).  
54 Different mechanisms such as static triggering (King et al., 1994), triggering due to afterslip  
55 (Barbot et al., 2009; Peng and Zhao, 2009), and dynamic triggering (Anderson et al., 1994; Hill  
56 et al., 1993; Kilb et al., 2000; Yun et al., 2019) can cause various earthquake migration patterns.  
57 For instance, King et al. (1994) discovered that the aftershocks of the 1992 Landers earthquake  
58 were distributed at sites where Coulomb stresses have risen. In a longer timescale, afterslip may  
59 have a more critical role in triggering aftershocks than static triggering. Barbot et al. (2009)  
60 observed greater moment release from afterslip than coseismic slip of the 2004 Parkfield

61 earthquake. The aftershocks of this earthquake migrated along the fault with logarithmic time  
62 since the mainshock, showing the distinct migration pattern of afterslip-triggered aftershocks  
63 (Peng and Zhao, 2009). In addition to aftershocks triggered by local mainshocks, dynamic  
64 triggering could also cause aftershocks by long-period waves. For instance, the 1992  $M_w$  7.3  
65 Landers earthquake triggered three magnitude 3.4+ events and numerous small events at  
66 distances of several hundred kilometers (Anderson et al., 1994). Prejean et al. (2004) observed  
67 that the remotely triggered seismicity initiated with the arrival of the surface wave of the 2002  
68  $M_w$  7.8 Denali Fault earthquake.

69 In addition to the tectonic process, anthropogenic activities such as fluid injection may  
70 also cause clear migration of earthquakes, which serve as one of the vital information to infer  
71 their inducing mechanisms. In the past decade, the rate of induced earthquakes has increased  
72 abruptly in the US and Canada (Atkinson et al., 2016; Bao and Eaton, 2016; Friberg et al., 2014;  
73 Holland, 2013) due to activities like wastewater disposal that are associated with hydrocarbon  
74 production. Hydraulic fracturing, a technique commonly used in stimulating fracture growth, can  
75 also trigger moderate ( $M_L$  3–5) and strong ( $M_L > 5$ ) earthquakes, causing substantial damage.  
76 Since 2010, China has been conducting shale gas exploration, drilling over 500 production wells  
77 in the Sichuan Basin (Tan et al., 2020). Meanwhile, the Sichuan Basin has experienced frequent  
78 earthquakes (Lei et al., 2019a; Yang et al., 2020; Wong et al., 2021; Zhou et al., 2021). The fluid  
79 injection may activate the local faults and lead to large earthquakes. For instance, the  $M_w$  5.7  
80 earthquake that occurred on June 17th, 2019, Changning, killed 13 people, injured more than 200  
81 people, and damaged numerous buildings, was considered as an interaction among hydraulic  
82 fracking, salt mining, and smaller magnitude earthquakes in the region (Lei et al., 2019b; Jia et  
83 al., 2020; Liu and Zahradník, 2020). In September and December 2019, two moderate  
84 earthquakes with magnitudes  $>5$  occurred in Weiyuan, killing four people and injuring 75 (Lei et  
85 al., 2019a; Wang et al., 2020; Sheng et al., 2020). These sequences illustrated the urgent need to  
86 closely monitor the seismicity induced by hydraulic fracturing and better understand the  
87 underlying triggering mechanisms.

88 Mapping out seismicity evolution in high resolution has been commonly used to infer the  
89 mechanisms driving earthquakes and their migrations for both natural earthquakes (Anderson et  
90 al., 1994; Peng and Zhao, 2009; Zhang et al., 2022; Zhu et al., 2022) and induced seismicity (Lei  
91 et al., 2017; Haffener et al., 2018; Grigoli et al., 2018). The typical approach to analyzing spatio-  
92 temporal migration relies on a spatial or temporal mark, such as a mainshock for natural  
93 earthquakes or industrial records for induced ones. Compared with natural earthquakes, induced  
94 seismicity is sometimes more challenging to investigate partly due to its small spatio-temporal  
95 scales and the necessity of including low magnitude earthquakes with limited accuracy of  
96 hypocenters. Despite these difficulties, many studies have conducted the temporal correlation  
97 between earthquake occurrence timings and injection records to link the induced seismicity with  
98 hydraulic fracturing (Haffener et al., 2018; Lei et al., 2017; Lei et al., 2019b; Meng et al., 2019;  
99 Tan et al., 2020). Some other studies have used earthquake hypocenters as a critical indicator to  
100 identify the induced earthquakes with large magnitude ( $M_L > 4$ ) (Grigoli et al., 2018; Sheng et  
101 al., 2020). Incorporating both spatial and temporal information, Johann and Shapiro (2020)  
102 applied a multidimensional cross-correlation technique to investigate the spatio-temporal  
103 relationship between induced seismicity and injection volumes. However, all the studies  
104 mentioned above are based on correlation with industrial activities, which are not entirely  
105 accessible to the public (Schultz et al., 2020). Therefore, a new methodology is demanded to  
106 map out seismicity migration without prior information.

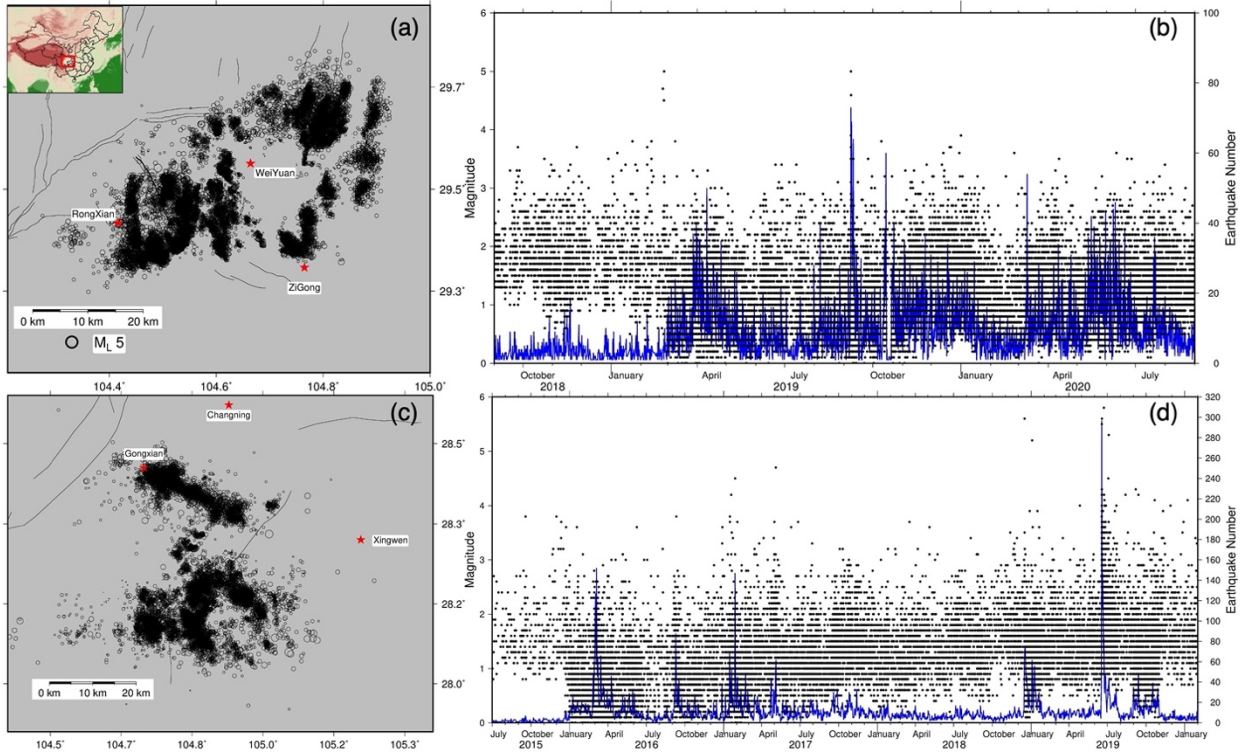
107 Here, focusing on induced earthquakes that often exhibit spatial clustering yet abrupt  
108 changes of low-magnitude events in a short period, we develop a deep-learning-based, automated  
109 method to extract anomalous spatial-temporal information from earthquake catalogs. Powered by  
110 deep learning, our method does not require prior knowledge (e.g., background seismicity rates  
111 from historical catalogs, industrial operation records) and thus is applicable for induced  
112 earthquakes. We first train our neural network from a well-identified induced earthquake  
113 sequence in the Changning shale gas block within the Sichuan Basin. Then we apply the trained  
114 network to the dataset in the Weiyuan shale gas block to identify anomalous changes in the  
115 pattern of seismicity. Moreover, due to the transferability of deep learning, our method has the  
116 potential to be applied to a broader area and detect abnormal changes in seismicity during natural  
117 earthquake sequences, including those associated with foreshock sequences or aftershock  
118 triggering.

## 119 **2. Catalog data and characteristics**

120 Our study region is located in the southern Sichuan Basin (Fig. 1), where several shale  
121 gas blocks have been rapidly developed since 2011. Among the shale gas blocks in Sichuan,  
122 Changning and Weiyuan blocks are the two major gas production sources (Zou et al., 2018).  
123 Since 2014, the pace of shale gas production has been accelerated, and frequent earthquakes,  
124 including events with magnitudes larger than five, have been reported (Meng et al., 2019; Yang  
125 et al., 2020; Zhou et al., 2021).

126 We first adopt an earthquake catalog in Weiyuan, which contains 24,719 earthquakes  
127 from September 2018 to August 2020 (Wong et al., 2021; Fig. 1a), bounded by longitudes  
128  $104.21^\circ$  and  $105^\circ$  and latitudes  $29.2^\circ$  and  $29.8^\circ$ . From 2018 to February 2019, seismic  
129 waveforms were recorded by nine short-period seismometers (Yang et al., 2020). From 2019 to  
130 2020, 14 additional seismometers were deployed in the region, bringing the total number of  
131 stations to 23. The phase data are picked by a machine-learning phase picker (Zhu and Beroza,  
132 2019), and earthquakes are relocated through the double-difference (HypoDD) algorithm  
133 (Waldhauser and Ellsworth, 2000).

134 The catalog in the Changning shale gas field is from Meng et al. (2019), who derived  
135 high-resolution earthquake locations from local temporary seismic stations. The catalog contains  
136 18,507 earthquakes from July 2015 to January 2020 (Fig. 1c) with magnitudes up to  $M_w$  4.7,  
137 bounded by longitudes  $104.2^\circ$  and  $105.4^\circ$  and latitudes  $27.8^\circ$  and  $28.6^\circ$ . Between February 2015  
138 to April 2017, 6 temporary seismometers were deployed, and additional 15 seismometers were  
139 added afterward. The stations were distributed evenly within and surrounding the study region,  
140 yielding a high-resolution catalog with a completeness magnitude of  $M_L$  1.1 that was derived  
141 from a double-difference tomographic method (tomoDD, Zhang and Thurber 2003).  
142 Furthermore, the seismicity in the catalog shows a close relationship with hydraulic fracturing  
143 (Meng et al., 2019), making it a reliable training dataset to extract the features of injection-  
144 induced earthquakes.



145

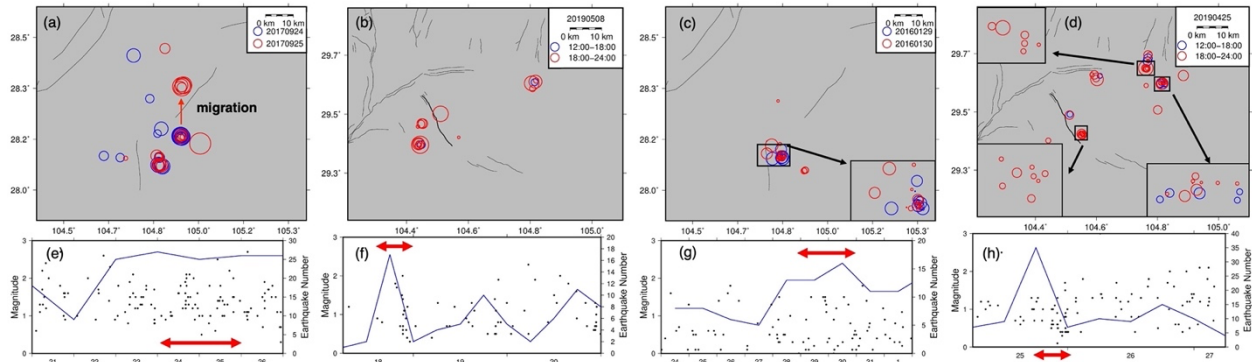
146 **Figure 1.** Earthquake distribution in our study areas Weiyuan (a) and Changning (c). (b) and (d)  
 147 shows the time series of earthquake numbers for Weiyuan and Changning over the entire study  
 148 period.

149 Both catalogs contain seismic features distinct from background seismicity. Here, we  
 150 define three types of behaviors as abnormal seismicity: (1) earthquake migration, (2) sudden, and  
 151 (3) gradual increase of earthquake number in small subregions (Figure 2). In the first scenario,  
 152 earthquake migration, the previous earthquake swarms vanish, and new swarms appear (Figure  
 153 2a), but the total number of earthquakes in the whole region does not change much (Figure 2e).  
 154 In the second scenario, a group of earthquakes may emerge quickly in a small region and then  
 155 vanish in a short term (Figure 2b), exhibiting a clear signature of temporal clustering (Figure 2f).  
 156 In contrast, the earthquake number may change gradually over time but overall maintain at a  
 157 high level for days (Figure 2g). We classify such phenomenon as type 3.

158 The coupling of spatial and temporal information in the catalogs complicates the  
 159 detection of individual clusters (Figure 1). For instance, the three types of abnormal features  
 160 could occur simultaneously in various subregions (Figure 2d & h). Therefore, we choose the  
 161 deep learning algorithm to solve this complexity. Additionally, the spatial transferability of deep  
 162 learning could enable the method to be applied to places beyond the training region, meaning  
 163 that we could apply the network to extract similar abnormal features in various regions. To  
 164 demonstrate, we use the Changning catalog to train the deep learning network and then use the  
 165 Weiyuan catalog to test the spatial transferability of the network.

166 In the two catalogs, we focus on the spatio-temporal changes in earthquake number and  
 167 epicenter to extract abnormal features. The magnitudes of the earthquakes are not used because  
 168 (1) most induced earthquakes have small magnitudes, and (2) large-magnitude earthquakes will

169 naturally become good references providing timings and locations for detailed investigations. We  
 170 do not use depth information since induced earthquakes caused by hydraulic fracturing are  
 171 usually concentrated in a specific depth range. Also, the usage of earthquake hypocenters  
 172 requires higher accuracy in event depths, which are however often not resolved as good as did  
 173 for epicenters.



174

175 **Figure 2.** Example of anomalous seismicity within a 2-day time window in Changning (a & c)  
 176 and 12-hour window in Weiyuan (b & d). Circles represent the locations and magnitudes of  
 177 earthquakes. (a) shows the example of earthquake migration, (b) shows the sudden change in  
 178 seismicity, (c) shows the gradual changes in seismicity in the region, and (d) shows the  
 179 combination of the second and the third scenarios. (e-h) show the earthquake magnitude and the  
 180 time series of earthquake numbers each day (a & c) or every 6 hours (b & d) in a longer time  
 181 window. The red arrows indicate the period of the figures above.

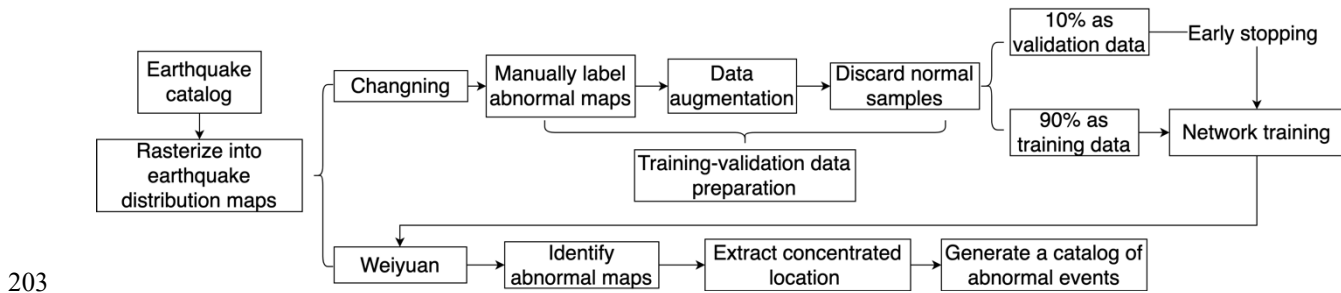
### 182 3 Method

183 Temporal and spatial changes in earthquake numbers have been widely used to illustrate  
 184 the causal relationship between anthropogenic activities and induced seismicity (Lei et al., 2017;  
 185 Lei et al., 2019a; Yang et al., 2020). Without a large magnitude earthquake or industrial records  
 186 as a reference, the abnormal increase in earthquake rates becomes essential to distinguish the  
 187 induced seismicity from the background. In Changning, the average seismic rate before hydraulic  
 188 fracturing was less than four events every three years from 1970 to 2014. From 2015 to 2017,  
 189 15,057 earthquakes with  $M_L > 0$  were identified after shale gas production began (Meng et al.,  
 190 2019). A similar phenomenon occurred in Weiyuan, with infrequent seismicity before mid-2015  
 191 and a dramatic increase in the number of earthquakes afterward (Yang et al., 2020).

192 Here, based on the variation of earthquake numbers, we automatically extract spatio-  
 193 temporal anomalous information based on deep learning technology (Fig. 3). The deep learning  
 194 network is designed to identify and extract the timing of abnormal events, and a post-process  
 195 procedure extracts the locations of abnormal events. More specifically, our method has three  
 196 main steps:

- 197 • Rasterizing an earthquake catalog into distribution maps that are discretized in space  
 198 and time.
- 199 • Applying the network to a sequence of consecutive maps to identify the abnormal  
 200 ones and their timings.

- 201 • Extracting the locations where the earthquakes are concentrated from each abnormal  
 202 map.



204 **Figure 3.** Diagram of the deep-learning-based framework described in the Method section.

### 205 3.1 Generating distribution maps

206 To generate distribution maps, we count the number of earthquakes in each grid with a  
 207 given temporal and spatial resolution. Here we set the spatial resolution as 2 kilometers, the  
 208 commonly recognized maximum diffusion range of an injection well (Atkinson et al., 2020).  
 209 Thus, the image sizes are  $59 \times 44$  in Changning and  $38 \times 33$  in Weiyuan. After rasterization, we  
 210 pad images with zeros to keep an identical size,  $75 \times 75$ , for each image. Apparently, the seismic  
 211 density determines the temporal resolution. A too-wide temporal resolution could cause many  
 212 timings to be abnormal, which violates our objective of saving manual practice. However, a too-  
 213 narrow time window might lead to missing some abnormal timings. In Changning, we rasterize  
 214 the catalog into daily distribution maps, while the temporal resolution for the Weiyuan catalog is  
 215 six hours from a trial-error process, and each map has its timing.

### 216 3.2 Principles of labeling anomalous seismicity and preparing the training set

217 The labeling of anomalous seismicity is based on the definition of three types of  
 218 abnormal behaviors (Fig. 2). The maps with migration and sudden increases are self-evident.  
 219 When the earthquake number increases gradually, we only consider the map with the local peak  
 220 as abnormal to reduce the number of detected events and the manual effort required for further  
 221 investigation. Although our objective is to detect the abnormal induced seismicity, we do not  
 222 exclude the anomalous events caused by large natural earthquakes because it will not hurt our  
 223 objective and could also provide unique abnormal seismic features to enrich the training set. For  
 224 labeling all the types of abnormal maps, we use a threshold of six, meaning all the abnormal  
 225 maps should have at least six earthquakes in a small cluster. The cluster size varies, and different  
 226 types of behavior might occur at the same time. For instance, one cluster is vanishing but still has  
 227 a large earthquake number, while another cluster suddenly appears in a different place. Due to  
 228 these complexities, deep learning technology is more appropriate for detecting abnormal events.  
 229 The label preparation is conducted iteratively. We first prepare the initial labels and train the  
 230 network. Then, we manually check the differences between the network's output and refine the  
 231 labels. For instance, the network can detect some missing abnormal events by manual labeling.  
 232 Further, for ambiguous events that we consider normal, we will reconsider them if the network  
 233 thinks differently. Such iterative progress would mitigate the manual error and subjectiveness in  
 234 the label preparation.

235 After label preparation, we integrate a series of consecutive maps and their labels to  
236 compose a training example. We move the temporal window by one image each step to make  
237 multiple training examples. The number of labels equals the number of consecutive maps minus  
238 one since the abnormality of the first map will not be determined without a prior map as a  
239 reference. The training set contains all the abnormal distribution maps in Changning from July  
240 2015 to January 2020, with 1624 distribution maps with 212 abnormal ones. Due to the  
241 imbalance between normal examples and abnormal ones, we randomly discard 1/3 of normal  
242 samples to balance the training data. From the training samples, we randomly choose 10% as the  
243 validation dataset. The validation dataset mitigates overfitting and adjusts hyperparameters such  
244 as the learning rate.

245 We use the data in Weiyuan from March to October 2019 as our test dataset. The test  
246 region is beyond the training region to test the spatial transferability of the network. Further, the  
247 test set can provide a more representative accuracy of the network than the training set since a  
248 high accuracy of the training set is expected. The preparation for the test set is the same as the  
249 training set. The test set includes 937 distribution maps with 154 abnormal ones.

250 We apply the data augmentation to increase the diversity of our training dataset and the  
251 generalization of the network while keeping the manual labeling of rasterized maps to a  
252 manageable level. We flip and rotate the distribution image by degrees ranging from  $45^\circ$  to  $315^\circ$   
253 with an interval of  $45^\circ$ . We also shift images vertically by 5 and 10 pixels and horizontally by  
254 steps ranging from 5 to 25 with an interval of 5 pixels. In the original training data, the  
255 earthquakes are located in the maps' central part. The earthquakes will sample more areas in the  
256 image domain by shifting images. All the augmentations are conducted independently and share  
257 the same list of labels.

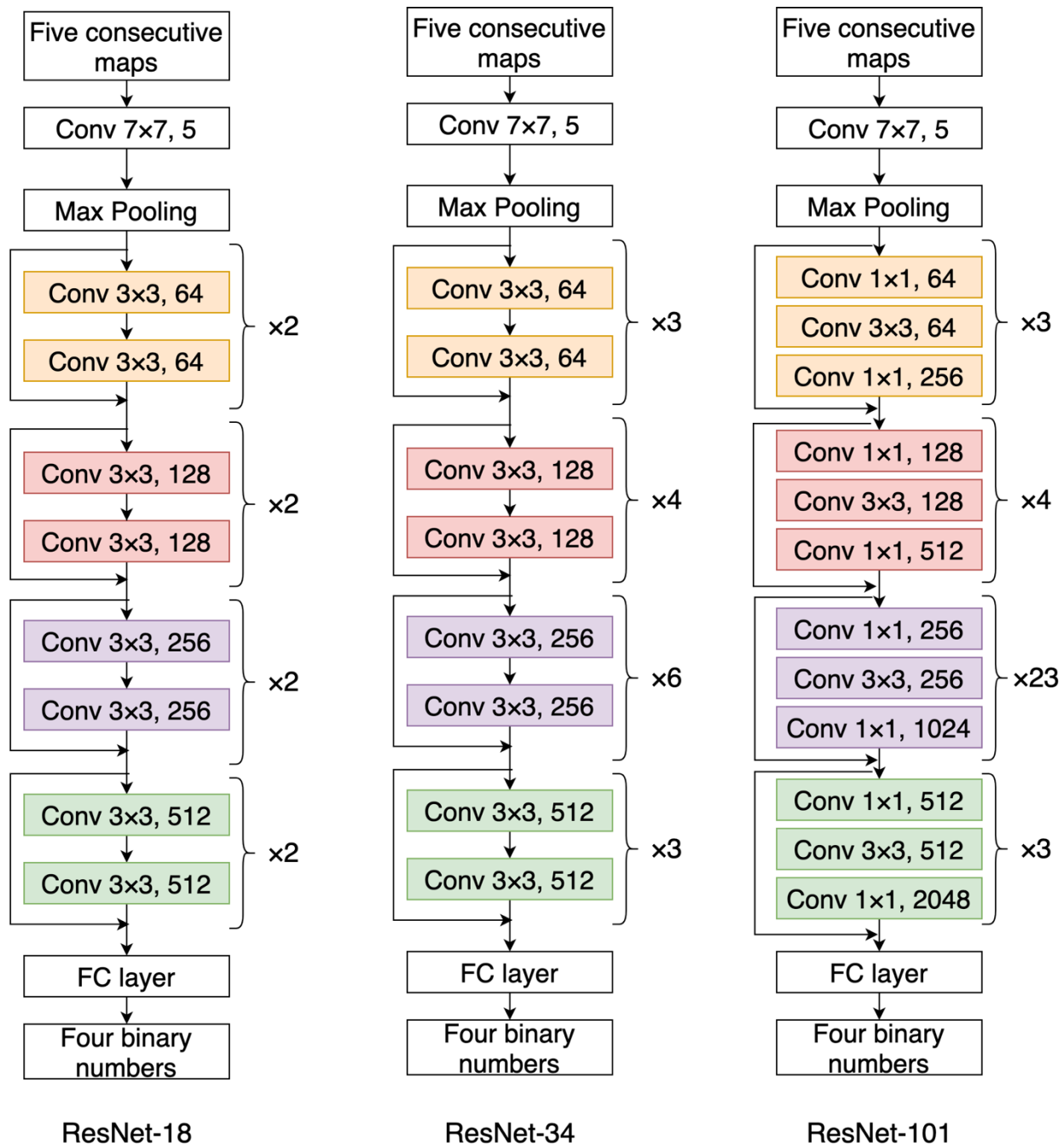
258 To further enrich the training dataset, we generate three types of artificial distribution  
259 maps. The first type has scatter distributions with an earthquake number less than two in a single  
260 pixel (Fig. S1a). The other two types are both superimposed on the first one. The second type has  
261 pixels with earthquake numbers larger than six (Fig. S1b). The third type has pixels where the  
262 earthquake number increases gradually in the same pixel, and the peak has more than six  
263 earthquakes (Movie S1). The maps from the second and the peak from the third types will be  
264 classified as anomalous maps, while the maps from the first type are normal ones.

### 265 **3.3 Deep learning network for identifying anomalous maps**

266 Deep learning has been widely applied in seismology, such as automating phase picking  
267 (Zhu and Beroza, 2019; Johnson et al., 2021), locating earthquakes (Zhang et al., 2020), and  
268 determining focal mechanisms in real-time (Kuang et al., 2021). Here, we adopt the idea of  
269 image classification to identify abnormal earthquake distribution maps. The conventional way of  
270 classifying images is to apply the deep learning network to a single image. The output would be  
271 a list of binary numbers indicating which class the image belongs to (He et al., 2016). Here, we  
272 apply the network to a sequence of distribution maps and output binary numbers indicating their  
273 abnormality, i.e., seismicity changes as defined above. To examine the effect of input map  
274 numbers, we use five, seven, and ten consecutive maps as the input.

275 Here, we use the ResNet deep learning architecture, which has achieved outstanding  
276 performance in image classification (He et al., 2016). ResNet includes a building block of  
277 residual learning (Fig. S2), which can avoid the typical problem that the accuracy becomes

278 saturated and degrades as the network depth increases. With such a design, ResNet allows to  
279 greatly increase the network depth and the learning capacity (He et al., 2016). Therefore, it could  
280 be applied to broader areas with more complex and diverse migration patterns, including natural  
281 earthquakes. ResNet has different branches with various numbers of blocks and layers. The more  
282 layers a network has, the more learning capability it contains. However, a too large network  
283 might yield overfitting issues, depending on the complexity level of the task. We examine the  
284 performance of ResNet-18, ResNet-34, and ResNet-101 (Fig. 4) and choose the best one.  
285 ResNet-18 has eight blocks, containing 17 convolutional layers; ResNet-34 has 16 blocks,  
286 containing 33 convolutional layers; ResNet-101 has 33 blocks, containing 100 convolutional  
287 layers. All the networks have a fully connected layer at the end of the architecture to generate the  
288 output labels. We use binary cross-entropy as the loss function and the stochastic gradient  
289 descent method as the optimizer. We also use the L2 regularization factor to mitigate the  
290 overfitting issue. We train the networks using different learning rates and L2 regularization  
291 factors and choose the most proper values for each network based on the final validation loss.  
292 The details of selecting the learning rate and L2 regularization factor are described in the  
293 supplementary material (Text S1).



295 **Figure 4.** Architecture of the ResNet-18, ResNet-34, and ResNet-101. Different colors represent  
 296 different building blocks. Conv  $3 \times 3$ , 64 means a convolutional layer with a  $3 \times 3$  kernel and 64  
 297 channels. FC means fully connected layers. The inputs are a sequence of distribution maps, and  
 298 outputs are binary numbers indicating the abnormality of the last four maps.

299 We start the training by initializing the network parameter using the He initialization  
 300 method (He et al., 2015). We adopt an early-stopping strategy to mitigate overfitting. After each  
 301 training epoch, we calculate the validation error and stop the training if the validation error starts  
 302 to increase for ten consecutive epochs. The inferencing after the training will sample a single

303 image multiple times since we move the temporal window by one image each time. We calculate  
 304 the averaged output for each image and consider it abnormal if the value is larger than 0.4, an  
 305 empirical threshold. The inferencing will be conducted on test data—the Weiyuan catalog from  
 306 March to October 2019—to quantify the accuracy of the networks. Specifically, we calculate the  
 307 F1 score on the test dataset to measure the consistency between manual labels and the network’s  
 308 predication and use it as the accuracy:

$$309 \quad F1 = \frac{TP}{TP + 0.5 \times (FN + FP)} \quad (1)$$

310 TP is true positive representing the maps that both the manual label and the network  
 311 consider as abnormal. FN is false negative, and FP is false positive. Both are network  
 312 misidentifications: FN is the network’s negative predication and TP is the positive predication.  
 313 We choose to use the F1 score since it focuses on the network’s ability to detect abnormal events  
 314 and considers both types of misidentifications. We conduct nine experiments that combine three  
 315 networks (ResNet-18, ResNet34, and ResNet-101) and three numbers (five, seven, and ten) of  
 316 input maps. We calculate the F1 score of each experiment and choose the one with the largest F1  
 317 score.

### 318 **3.4 Extracting anomalous locations from the identified maps**

319 The post-processing procedure further extracts the anomalous locations and generates a  
 320 catalog of abnormal events. For the identified abnormal maps, we apply a thresholding method to  
 321 extract the location with concentrated earthquake distribution. We first filter the image with a  
 322  $3 \times 3$  matrix of ones to sum up all the values in the surrounding pixels. Second, we extract two  
 323 sets of locations: (1) the locations with a value larger than the threshold (six) in the filtered maps  
 324 and (2) the locations in the original maps where the pixel value is larger than half of the  
 325 threshold. Third, we take the intersection of the two location sets as the abnormal locations.  
 326 Instead of using a single threshold, these processes could extract locations of clusters of various  
 327 sizes. Moreover, the post-processing could filter out some misidentified maps with no  
 328 concentrated earthquakes, further increasing our method’s accuracy. Finally, we generate a  
 329 catalog of abnormal events by taking each abnormal location at a specific timing as an event.

## 330 **4. Results**

331 The key results are presented in the following order: (1) F1-score-based comparison  
 332 among the nine experiments as in Table 1; (2) the application on the Weiyuan catalog; (3) the  
 333 application on the Changning catalog.

### 334 **4.1 The best network based on the F1 score of the test set**

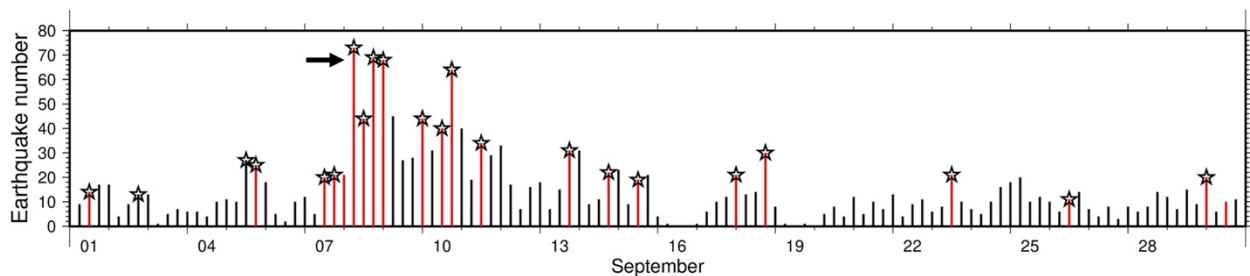
335 **Table 1.** F1 scores of the nine experiments. TP means true positive, and FP means false positive.

	Five maps	Seven maps	Ten maps
ResNet-18	TP: 141	TP: 128	TP: 115
	FP: 58	FP: 28	FP: 16
	F1: 0.79	F1: 0.81	F1: 0.79

ResNet-34	<b><u>TP: 137</u></b>	TP: 136	TP: 122
	<b><u>FP: 19</u></b>	FP: 30	FP: 24
	<b><u>F1: 0.87</u></b>	F1: 0.84	F1: 0.80
ResNet-101	TP: 127	TP: 112	TP: 132
	FP: 13	FP: 12	FP: 32
	F1: 0.85	F1: 0.79	F1: 0.82

336 We estimate the accuracy of the nine experiments by comparing manual labels and  
 337 network predications. The uncertainties estimation is conducted in Weiyuan, a different shale gas  
 338 field than Changning where the training was conducted, which can therefore provide a more  
 339 representative estimation of the model's accuracy. Table 1 summarizes the F1 score of the nine  
 340 experiments with higher F1 scores showing the better results. All the experiments have similar  
 341 and promising performances, while ResNet-34 is better than the other two branches for our task.  
 342 More convolutional layers lead to greater learning capability. However, the complexity level is  
 343 limited due to the small input image size ( $75 \times 75$ ). Therefore, a too deep network could easily  
 344 overfit the training data. In other words, ResNet-101 has a larger learning capability than what  
 345 this task needs and the overfitting issues make the performance of ResNet-101 worse than  
 346 ResNet-34. However, ResNet-101 might be more appropriate when applying to datasets that  
 347 have longer durations and larger special coverage (e.g., natural earthquake catalogs). The best  
 348 experiment here is the combination between ResNet-34 and five consecutive maps, which is used  
 349 to derive all the following results. As an example, Fig. 5a shows the visual comparison between  
 350 manual labels and the predications of the best network. The two datasets are consistent with each  
 351 other in the number of days when we found anomalous seismicity in September 2019. The visual  
 352 comparison in other periods of the test data is shown in Fig. S3.

353 Using these identified timings, we can then find the location where the anomalous  
 354 seismicity occurred (Fig. 5b). Some earthquakes, e.g., those in the east of the study region  
 355 associated with the 2019  $M_S$  5.4 earthquake, are spatially and temporally clustered (Fig. 5b).  
 356 However, there are spatially separated locations where seismicity nearly emerged at the same  
 357 time (Fig. 5b), making it difficult to automatically identify by traditional methods.



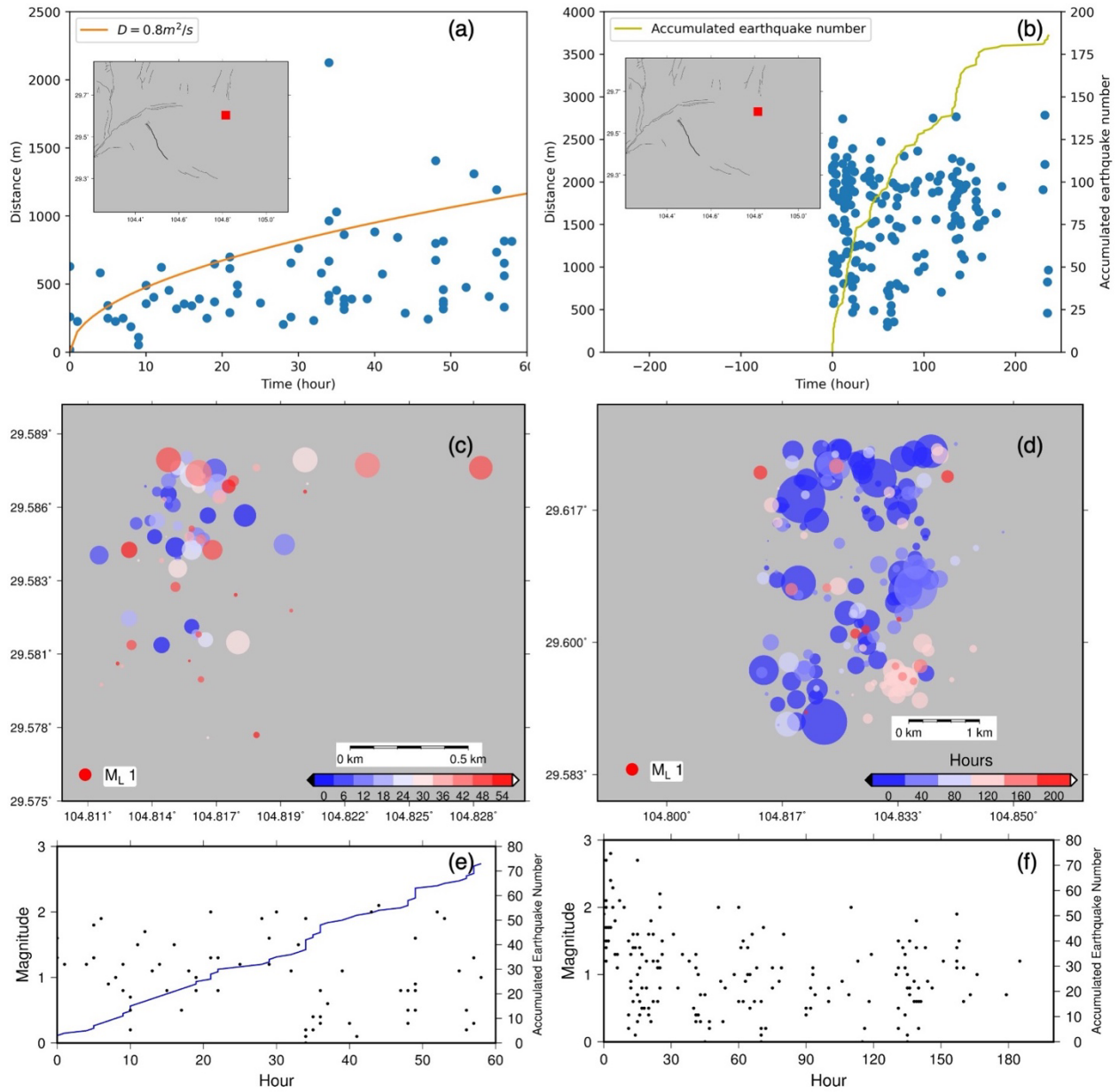
358

359 **Figure 5.** Comparison between manually picked anomalous timings and network identifications  
 360 in Weiyuan, September 2019. The red bars represent the manually identified anomalous timings.

361 The stars show the identified timings by the well-trained network. The arrow points to the  
362 anomalous seismicity caused by the  $M_s$  5.4 earthquake on September 8th, 2019.

#### 363 **4.2 Application on the Weiyuan catalog**

364 In Weiyuan, we condense the catalog from 24,719 events to 831 abnormal ones after  
365 running the detection by our trained network. The locations and timings in the condensed  
366 anomalous catalog provide critical information for further investigation of the triggering  
367 mechanisms of each earthquake cluster. For example, we identify an anomalous cluster starting  
368 from April 30th, 2019, in northeastern Weiyuan (Fig. 6a). Using a 60-hour temporal window and  
369 a 2-km spatial grid, we find that earthquakes near the anomalous event show a distinct spatio-  
370 temporal pattern (Fig. 6a, c, and e). Most earthquakes were within the pressure diffusion front  
371 with a hydraulic diffusivity of 0.8 m<sup>2</sup>/s, which is consistent with the value estimated in the  
372 region (Wong et al., 2021; Sheng et al., 2022), indicating that this earthquake swarm is likely  
373 driven by pore pressure diffusion. The other example is a cluster starting from August 08th,  
374 2019, in Weiyuan (Fig. 6b). Before August 08th, 2019, there were no earthquakes around the  
375 anomalous location (2 km spatial coverage), but the earthquake number increased drastically  
376 later (Fig. 6b). This cluster contains no events with magnitude larger than 3 (Fig. 6f), and the  
377 magnitude-time pattern does not suggest an aftershock sequence.

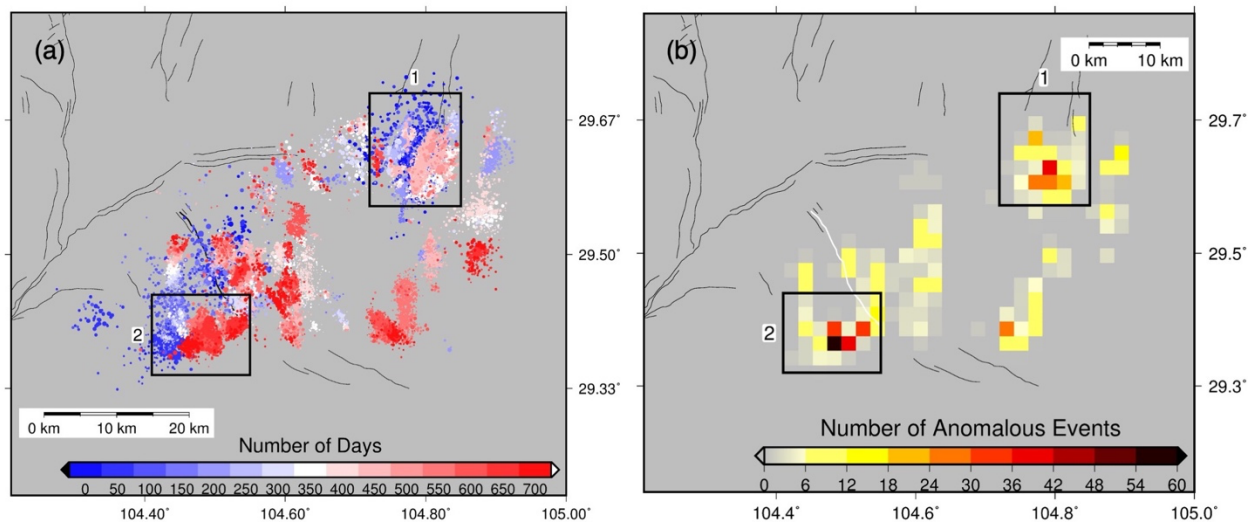


378

379 **Figure 6.** Two examples of identified anomalous earthquake clusters in Weiyuan. (a) shows a  
 380 cluster occurred on April 30th, 2019, and was potentially driven by pore pressure diffusion. The  
 381 red block in the map indicates the location of the cluster. (b) shows a sequence occurred on  
 382 August 08th, 2019, and the earthquake number increased dramatically. The red blocks in the  
 383 maps of (a) and (b) indicate the locations of the clusters. (c) and (e) show the seismicity of the  
 384 cluster in (a), while (d) and (f) indicate the one in (b). Both clusters have no large-magnitude  
 385 earthquakes.

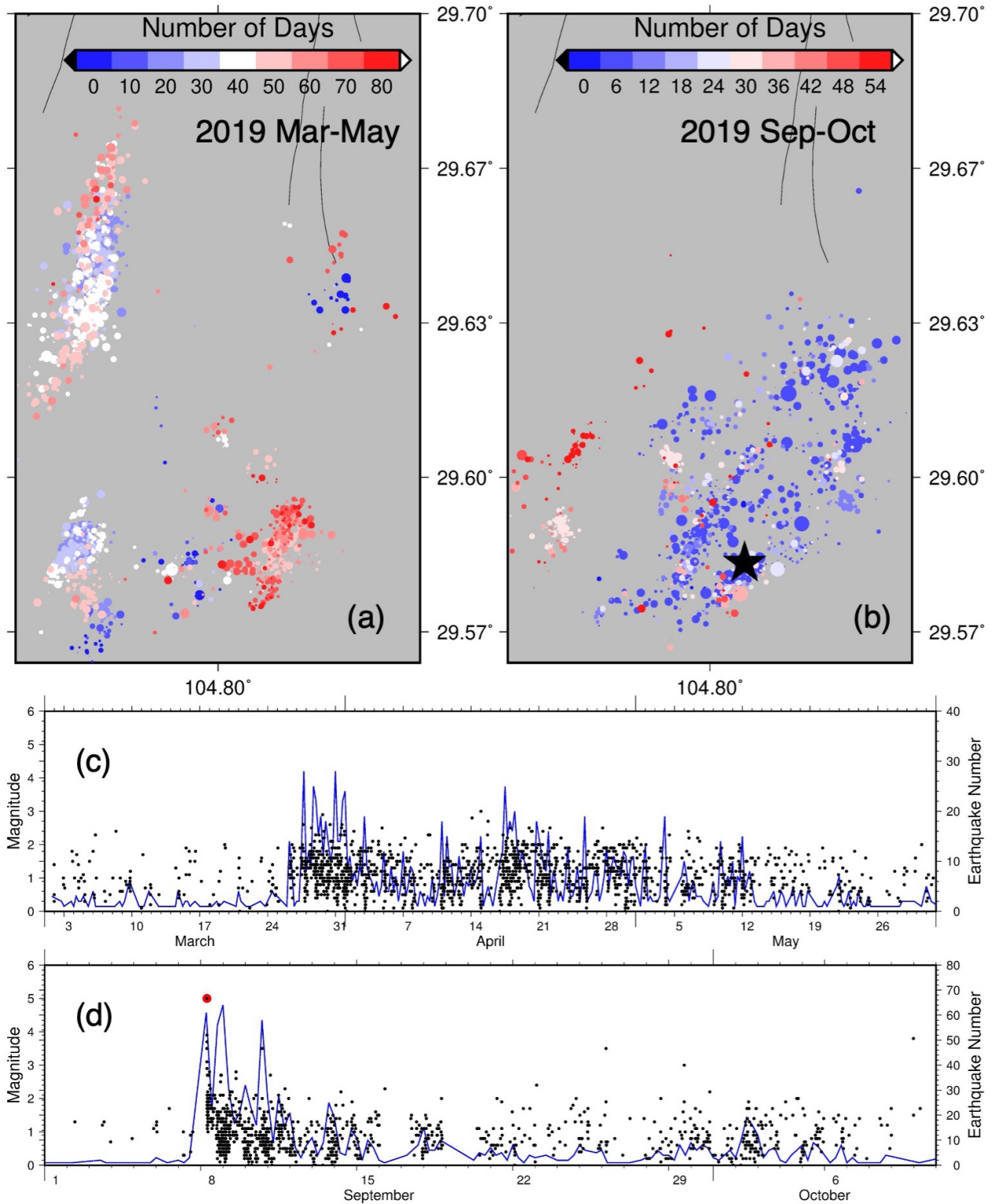
386 In addition to detecting locations and timings for individual clusters, the condensed  
 387 catalog could provide insights into the overall earthquake migration during the entire study  
 388 period (Movie S2). To illustrate, we count the total number of “anomalous” events in each grid  
 389 to generate a hot map of anomalous seismicity (Fig. 7b), in which a few distinct subregions can

390 be identified in Weiyuan (Fig. 7b). In comparison, identifying such “anomalous” subregions was  
 391 not straightforward in a traditional map of seismicity, despite that the earthquakes were colored  
 392 by their occurrence times (Fig. 7a). For instance, we identify one subregion (subregion 1) on the  
 393 hot map (Fig. 7b), where numerous seismicities occurred in the subregion within two years (Fig.  
 394 7a). As identified by our network, the anomalous seismicities were concentrated from March to  
 395 May and September 2019, respectively (Fig. 8). From March to May 2019, seismicity in  
 396 subregion 1 clearly exhibited a few clusters, emerging at different times (Fig. 8a). But there were  
 397 no earthquakes with magnitudes larger than 3 (Fig. 8c). In September 2019, an  $M_S$  5.4  
 398 earthquake occurred in the subregion, leading to a group of aftershocks that were identified by  
 399 our neural network (Fig. 8b & d). In the west of the study region, we also identified one  
 400 subregion 2 (Fig. 7), which exhibited two anomalous behaviors from April to July 2020 (Fig. 9).  
 401 First, an earthquake cluster emerged in the northeastern part of subregion 2 (blue dots in Fig. 9a)  
 402 and lasted until the end of April (Fig. 9b). After a few days of a few earthquakes (Fig. 9b),  
 403 numerous earthquakes started to occur in the central part of the subregion and then migrated  
 404 towards its northeast, northwest, and southwest directions.



405

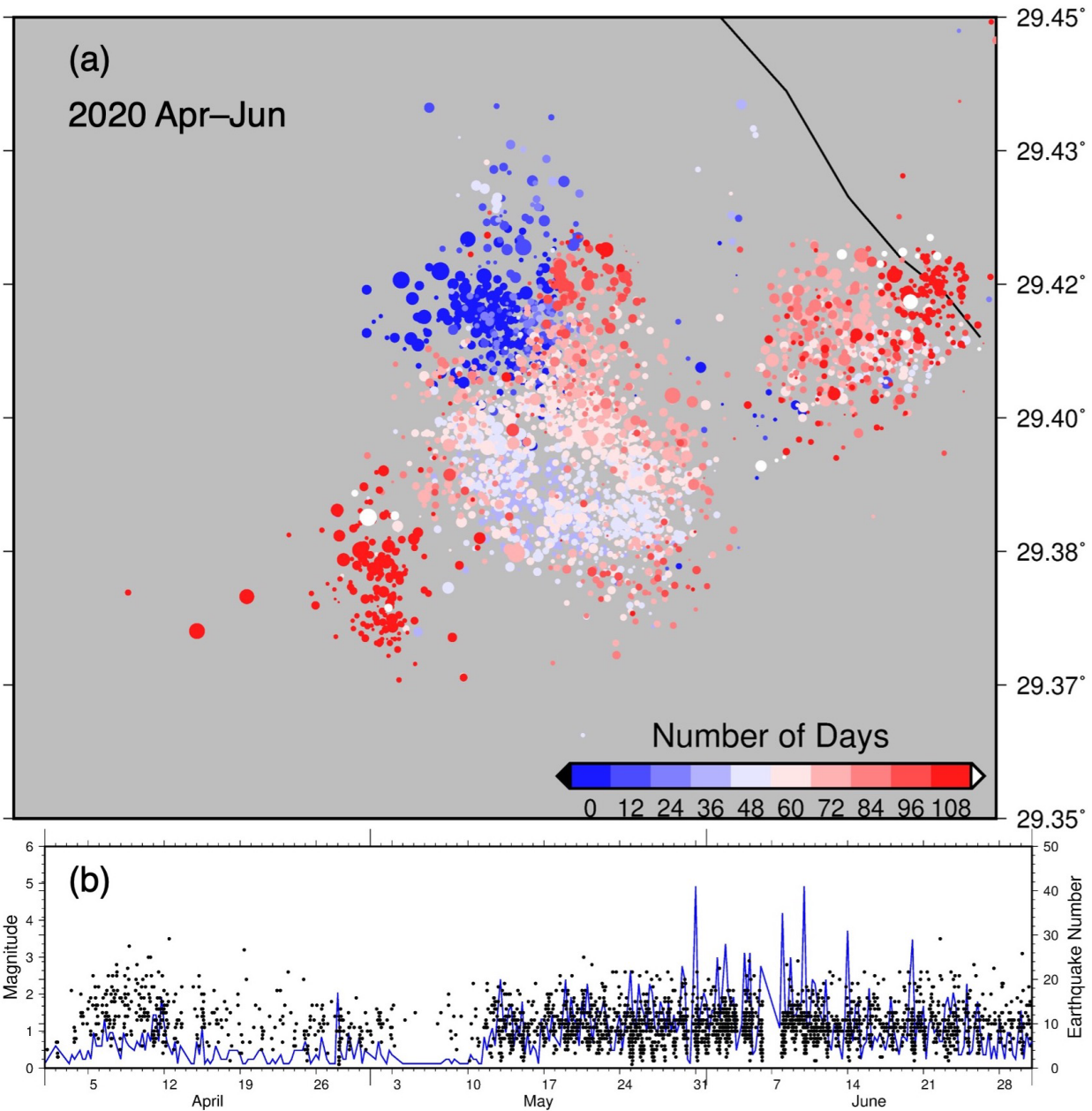
406 **Figure 7.** The density of abnormal seismicity in Weiyuan. (a) shows the seismicity of the entire  
 407 Weiyuan catalog. (b) a hot map of our identified “abnormal” regions, showing the total number of  
 408 anomalous events in each grid. The subregions are shown as black boxes and are identified based  
 409 on the density of abnormal events.



410

411 **Figure 8.** Seismicity in subregion 1 of Weiyuan during abnormal periods. (a) and (b) show the  
 412 seismicity in subregion 1 from Mar to May 2019 and from Sep to Oct 2019, respectively. (c) and  
 413 (d) are the corresponding time series of (a) and (b), showing the earthquake magnitudes and

414 earthquake numbers every six hours in subregion 1. The  $M_S$  5.4 earthquake is shown as the black  
 415 star in (b) and the red dot in (c).



416

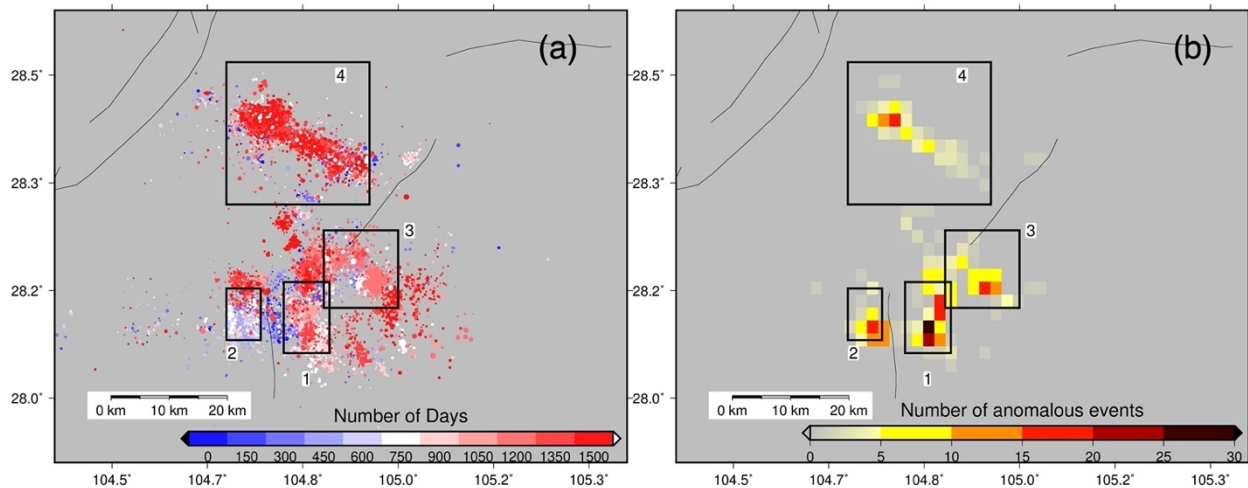
417 **Figure 9.** Seismicity in subregion 2 of Weiyuan from April to June 2020 (a) and the  
 418 corresponding time series of earthquake magnitudes and earthquake numbers every six hours (b).  
 419 The northeastern cluster (blue) occurred in April, and the other cluster started to emerge in May  
 420 and migrated in three directions afterward.

#### 421 4.2 Application on the Changing catalog

422 After training our network from a subset of seismicity in Changing, we then conduct the  
 423 network detection and condense the catalog from 18,507 events to 498 based on the manually

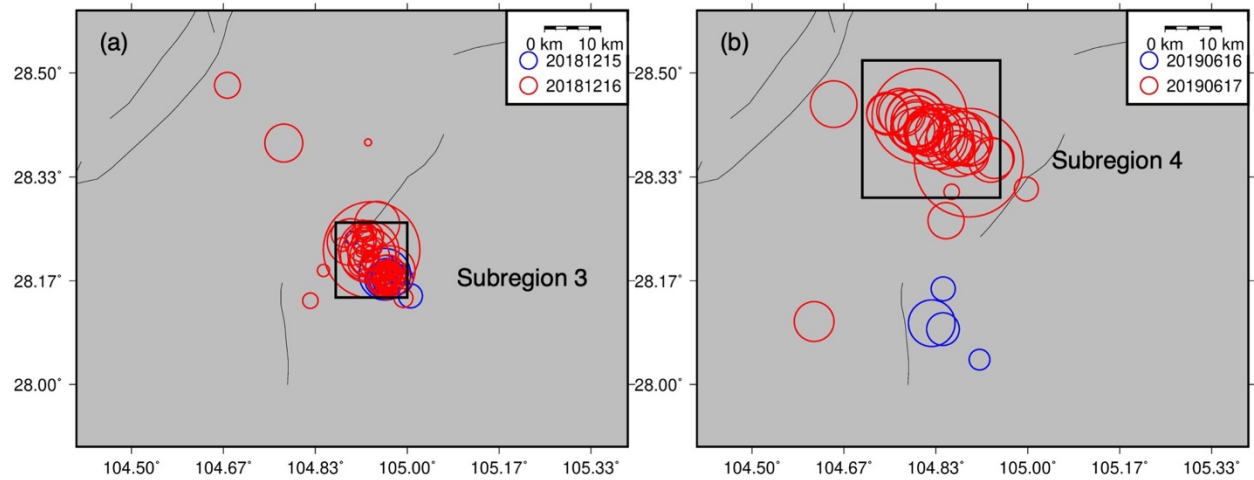
424 identified labels. In Changning, the event locations were usually concentrated in small  
 425 subregions for several months (Movie S3). The hot map of anomalous seismicity in Changning  
 426 shows four distinct subregions (Fig. 10). For instance, from February to April 2016, anomalous  
 427 locations were always in subregion 1, forming two obvious earthquake clusters in the northern  
 428 and southern parts (Fig. S4). From April to May 2017, subregion 1 became active again,  
 429 exhibiting a cluster in the central zone. In subregion 2, numerous clusters emerged in September  
 430 2016 and from January to February 2017. These clusters have no earthquakes with magnitudes  
 431 larger than five and no distinct migration features (Fig. S5). It was suggested that the anomalous  
 432 seismicity in subregion 2 was likely caused by hydraulic fracturing operations, which happened  
 433 from 3rd September to 8th October 2016 and from 12th to 19th January 2017, respectively  
 434 (Meng et al., 2019).

435 In addition to anomalous low-magnitude-induced seismicity, our method could also  
 436 detect anomalies caused by large earthquakes and their aftershocks. For instance, our method  
 437 detects the anomalies in seismicity caused by an  $M_w$  5.2 earthquake on December 16th, 2018, in  
 438 subregion 3 (Lei et al., 2019b) and an  $M_w$  5.8 earthquake that occurred on June 17th, 2019, in  
 439 subregion 4 (Fig. 11). Furthermore, the aftershocks of the large earthquakes could also cause the  
 440 proliferation of earthquake numbers. Therefore, the anomalous event continuously occurred in  
 441 subregion 3 from December 2018 to January 2019 (Fig. 12a & c) and in subregion 4 from June  
 442 to July 2019 (Fig. 12b & d). Although it is not our primary motivation to detect aftershocks and  
 443 practically it is not necessary to use such an algorithm because the large earthquakes already  
 444 serve as landmarks, the ability to detect anomalies caused by large-magnitude earthquakes shows  
 445 the feasibility of applying our algorithm in natural earthquake sequences. It also demonstrates the  
 446 effectiveness of using earthquake numbers without magnitudes and depth.



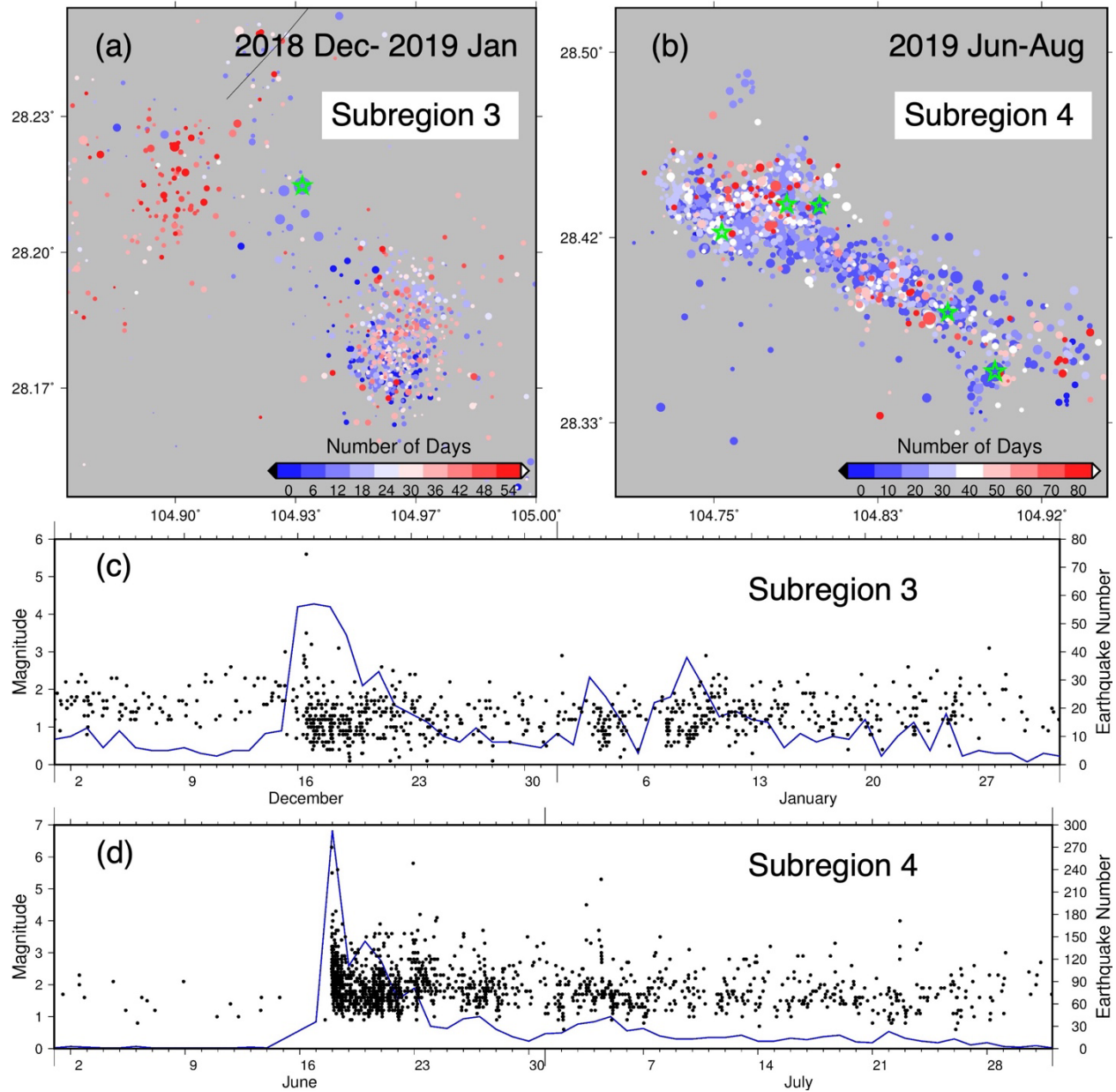
447

448 **Figure 10.** The density of abnormal seismicity in Changning. (a) shows the seismicity of the  
 449 entire Changning catalog. (b) hot map of abnormal seismicity, showing the total number of  
 450 anomalous events in each grid. The subregions are shown as black boxes and are identified based  
 451 on the density of abnormal events.



452

453 **Figure 11.** Anomalies caused by large-magnitude earthquakes in Changning. (a) shows the  
 454 anomaly on December 16<sup>th</sup>, 2018 in subregion 3. (b) shows the anomaly on June 17<sup>th</sup>, 2019 in  
 455 subregion 4. The circles in the legend box indicate the  $M_L$  1 earthquakes.



456

457 **Figure 12.** Seismicity in subregions 3 and 4 of Changning. (a) and (b) show the seismicity in  
 458 subregions 3 and 4 during their active period, respectively. (c) and (d) are the corresponding time  
 459 series of (a) and (b), showing the earthquake magnitudes and daily earthquake numbers in  
 460 subregions 3 and 4. The abnormal seismicities in both subregions 3 and 4 are triggered by large  
 461 earthquakes, shown as green stars in both (a) and (b).

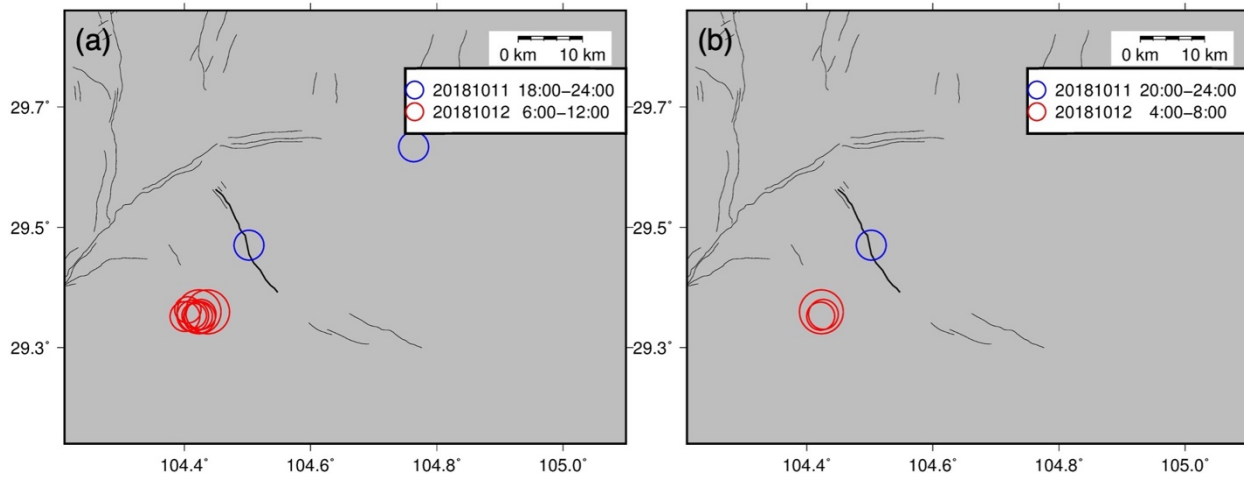
## 462 5. Discussion

### 463 5.1 Choosing the appropriate time interval

464 The choice of temporal resolution directly impacts the results, as the temporal density of  
 465 earthquakes determines the time interval of distribution maps. A large temporal resolution could

466 cause a large proportion of abnormal timings, while a too-small interval could miss some  
 467 abnormal timings. Here, we test the effect of the time interval for the Weiyuan catalog by setting  
 468 it as 24 and 4 hours, respectively, and compare it with our optimal 6-hour interval. For the 24-  
 469 hour interval, we identify 315 abnormal timing from 724 distribution maps. While most of the  
 470 reported timings were correct, the large proportion of anomalous maps violates our objective of  
 471 saving manual practice. In addition, the reported timings are less precise than using a six-hour  
 472 interval. In comparison, we condense the original catalog to 572 events when using the 4-hour  
 473 interval, less than the number (831) using the 6-hour interval. The 4-hour interval misses some  
 474 events because a shorter temporal interval dilutes the earthquake distribution for each map, and  
 475 some changes are not intense enough to be detected (Fig. 13b).

476 The results of the above test show that the choice of time interval to generate the  
 477 distribution maps can lead to a trade-off between the accuracy of reported timing and the amount  
 478 of manual practice. To overcome this, we may choose the strategy of adaptive time interval, i.e.,  
 479 find the anomalous timing in a relatively large time window first and then use a finer temporal  
 480 resolution. Furthermore, the absolute value of the time interval is subject to the total number of  
 481 earthquakes in a selected region, which depends on the background seismicity rate in the region  
 482 and the total duration of the catalog. For induced earthquakes, the study region and catalog  
 483 duration are usually selected according to the area of interest and time scales of industrial  
 484 activities. Therefore, the temporal resolution in our algorithm can be set and adjusted subject to  
 485 research focus.



486

487 **Figure 13.** Example of missing events due to the finer temporal resolution. (a) is identified as  
 488 abnormal but (b) is not because the changes in (b) are not intense enough. The circles in the  
 489 legend box indicate the  $M_L$  1 earthquakes.

## 490 5.2 Potential applications on natural earthquakes

491 Compared with induced earthquakes in the same term, catalogs of natural earthquakes  
 492 may have fewer earthquake numbers and thus a lower frequency of anomalies. However, our  
 493 algorithm can be directly applied on detecting “anomalous” changes in natural earthquakes. As  
 494 demonstrated by the aftershock sequences of the 2019  $M_w$  5.8 Changning and the 2018  $M_w$  5.2  
 495 Xingwen earthquakes, our algorithm is effective in detecting such changes in the amount of  
 496 seismicity in a relatively small region. Although it is not necessary to identify the emergence of

497 aftershocks with such an advanced technique, it may be applicable to investigate detailed  
498 aftershock evolution provided that some well-identified training datasets are available.

499 As we do not need to include magnitude information of earthquakes, it is obvious that our  
500 algorithm can be effective to identify earthquake swarms, an earthquake sequence in which no  
501 clear large-magnitude events (mainshock) exist. Normally earthquake swarms have been  
502 considered associated with fluid migration (Shelly et al., 2013); thus, mapping out swarms may  
503 advance our understanding of subsurface fluid transportation.

504 In addition, earthquakes may exhibit in foreshock-mainshock sequences, i.e., a series of  
505 small magnitudes preceding a large event in a time window from days to weeks (Kato and  
506 Nakagawa, 2014; Yao et al., 2020; Zhang et al., 2022; Zhu et al., 2022). Indeed, nearly 50% of  
507 large earthquakes had foreshocks, particularly for interplate events (Jones and Molnar, 1976;  
508 Bouchon et al., 2013). Despite the mechanisms driving foreshocks remain controversial (Zhu et  
509 al., 2022), foreshocks have been considered as the most reliable precursors that are hopeful for  
510 earthquake prediction. Because foreshocks often have low magnitudes, similar to the earthquakes  
511 used in this study, it is anticipated that our algorithm is capable of detecting the foreshock  
512 migration.

513 However, it is extremely challenging to recognize an ongoing foreshock sequence  
514 (Brodsky and Lay, 2014). Although our algorithm is able to identify an emerging earthquake  
515 sequence, it is a well-known difficult problem to distinguish them from the background  
516 seismicity. If there are well-recorded catalogs of background seismicity and large events with  
517 profound foreshock sequences, we may train our network to learn their features, respectively.  
518 Should there be distinct features between events leading to large earthquakes and these  
519 background ones, our network is hopeful to gain the capability of labeling potential foreshock  
520 sequences. The network's generalization ability of course needs to be tested in various regions  
521 and should be done in future studies.

### 522 **5.3 Limitations and possible solutions**

523 Although our method achieves promising results in the Sichuan Basin, it has several  
524 limitations. First, the network might fail to identify small-distance migration, depending on the  
525 spatial grid in our model and the location resolution of the training catalog. Second, when  
526 anomalous seismicity occurs frequently, the network might not automatically pick the precise  
527 onset of the anomaly, depending on the temporal resolution. These two cases are caused by the  
528 leak of corresponding training examples. The Changning catalog does not contain enough cases  
529 where anomalous seismicity migrated in a small distance or occurred frequently. Including more  
530 catalogs into the training data could increase the method's generalization and accordingly help to  
531 solve these misidentifications. Third, the current study does not consider the hypocenter depth of  
532 earthquakes due to the difficulties of visualizing 3-D matrixes and preparing the training labels.  
533 With more manual practice and higher catalog accuracy in the future, we could consider depth  
534 information in the network.

### 535 **6. Conclusion**

536 This study designs a novel method based on deep learning to automate the detection of  
537 anomalous seismicity. The detected locations and timings provide important information for  
538 investigating the triggering mechanisms of each earthquake cluster. Our approach could  
539 condense a large earthquake catalog to a focused catalog containing only anomalous events,

540 saving intensive manual practice. Based on the condensed catalogs, our further analysis reveals  
541 seismically abnormal subregions in the Changning and Weiyuan shale gas field and their  
542 corresponding active periods. In addition to the anomalous seismicity caused by anthropic  
543 activities, the method could also detect anomalies caused by large natural earthquakes. Owing to  
544 the large learning capability of deep learning, we could apply the method to broader areas with  
545 more complex and diverse earthquake migration patterns.

#### 546 **Acknowledgment:**

547 This study is supported by Natural Science Foundation of China (U2139203), Hong  
548 Kong Research Grants Council (14303721), CRIMS and Direct Grants from Faculty of Science  
549 at the Chinese University of Hong Kong. We also thank Dr. Lingyuan Meng for providing the  
550 Changning catalog, Jeremy Wing Ching Wong and Jinping Zi for providing the Weiyuan  
551 catalog.

#### 552 **Open Research:**

553 The catalogs and codes are available on  
554 <https://github.com/enzezhang/DLSeismicAnomaly>.

#### 555 **Reference**

- 556 Anderson, J. G. (1994). Seismicity in the western Great Basin apparently triggered by the  
557 Landers, California, earthquake, 28 June 1992. *Bulletin - Seismological Society of America*,  
558 *84*(3), 863–891.
- 559 Atkinson, G. M., Eaton, D. W., Ghofrani, H., Walker, D., Cheadle, B., Schultz, R., et al. (2016).  
560 Hydraulic fracturing and seismicity in the western Canada sedimentary basin. *Seismological*  
561 *Research Letters*, *87*(3), 631–647. <https://doi.org/10.1785/0220150263>
- 562 Atkinson, G. M., Eaton, D. W., & Igonin, N. (2020). Developments in understanding seismicity  
563 triggered by hydraulic fracturing. *Nature Reviews Earth and Environment*, *1*(5), 264–277.  
564 <https://doi.org/10.1038/s43017-020-0049-7>
- 565 Bao, X., & Eaton, D. W. (2016). Fault activation by hydraulic fracturing in western Canada.  
566 *Science*, *354*(6318), 1406–1409. <https://doi.org/10.1126/science.aag2583>
- 567 Barbot, S., Fialko, Y., & Bock, Y. (2009). Postseismic deformation due to the  $M_w$  6.0 2004  
568 Parkfield earthquake: Stress-driven creep on a fault with spatially variable rate-and-state  
569 friction parameters. *Journal of Geophysical Research: Solid Earth*, *114*(7), 1–26.

- 570 <https://doi.org/10.1029/2008JB005748>
- 571 Bouchon, M., Durand, V., Marsan, D., Karabulut, H., & Schmittbuhl, J. (2013). The long  
572 precursory phase of most large interplate earthquakes. *Nature Geoscience*, 6(4), 299–302.  
573 <https://doi.org/10.1038/ngeo1770>
- 574 Brodsky, E. E., & Lay, T. (2014). Recognizing foreshocks from the 1 April 2014 Chile  
575 earthquake. *Science*, 344(6185), 700–702. <https://doi.org/10.1126/science.1255202>
- 576 Freed, A. M. (2005). Earthquake triggering by static, dynamic, and postseismic stress transfer.  
577 *Annual Review of Earth and Planetary Sciences*, 33, 335–367.  
578 <https://doi.org/10.1146/annurev.earth.33.092203.122505>
- 579 Friberg, P. A., Besana-Ostman, G. M., & Dricker, I. (2014). Characterization of an earthquake  
580 sequence triggered by hydraulic fracturing in Harrison county, Ohio. *Seismological  
581 Research Letters*, 85(6), 1295–1307. <https://doi.org/10.1785/0220140127>
- 582 Grigoli, F., Cesca, S., Rinaldi, A. P., Manconi, A., López-Comino, J. A., Clinton, J. F., et al.  
583 (2018). The November 2017  $M_w$  5.5 Pohang earthquake: A possible case of induced  
584 seismicity in South Korea. *Science*, 360(6392), 1003–1006.  
585 <https://doi.org/10.1126/science.aat2010>
- 586 Haffener, J., Chen, X., & Murray, K. (2018). Multiscale Analysis of Spatiotemporal Relationship  
587 Between Injection and Seismicity in Oklahoma. *Journal of Geophysical Research: Solid  
588 Earth*, 123(10), 8711–8731. <https://doi.org/10.1029/2018JB015512>
- 589 He, K., Zhang, X., Ren, S., & Sun, J. (2015). Delving deep into rectifiers: Surpassing human-  
590 level performance on imagenet classification. *Proceedings of the IEEE International  
591 Conference on Computer Vision, 2015 Inter*, 1026–1034.  
592 <https://doi.org/10.1109/ICCV.2015.123>

- 593 He, K., Zhang, X., Ren, S., & Sun, J. (2016). Deep residual learning for image recognition. In  
594 *Proceedings of the IEEE Computer Society Conference on Computer Vision and Pattern*  
595 *Recognition* (Vol. 2016-Decem, pp. 770–778). IEEE Computer Society.  
596 <https://doi.org/10.1109/CVPR.2016.90>
- 597 Hill, D. P., Reasenber, P. a, Michael, a, Arabaz, W. J., Beroza, G., Brumbaugh, D., et al.  
598 (1993). Remotely Triggered. *Science*, *260*(June), 1617–1623.
- 599 Holland, A. A. (2013). Earthquakes triggered by hydraulic fracturing in south-central Oklahoma.  
600 *Bulletin of the Seismological Society of America*, *103*(3), 1784–1792.  
601 <https://doi.org/10.1785/0120120109>
- 602 Jia, K., Zhou, S., Zhuang, J., Jiang, C., Guo, Y., Gao, Z., et al. (2020). Nonstationary background  
603 seismicity rate and evolution of stress changes in the changning salt mining and shale-gas  
604 hydraulic fracturing region, Sichuan basin, China. *Seismological Research Letters*, *91*(4),  
605 2170–2181. <https://doi.org/10.1785/0220200092>
- 606 Johann, L., & Shapiro, S. A. (2020). Understanding vectorial migration patterns of wastewater-  
607 induced earthquakes in the united states. *Bulletin of the Seismological Society of America*,  
608 *110*(5), 2295–2307. <https://doi.org/10.1785/0120200064>
- 609 Johnson, S. W., Chambers, D. J. A., Boltz, M. S., & Koper, K. D. (2021). Application of a  
610 convolutional neural network for seismic phase picking of mining-induced seismicity.  
611 *Geophysical Journal International*, *224*(1), 230–240. <https://doi.org/10.1093/gji/ggaa449>
- 612 Jones, L., & Molnar, P. (1976). Frequency of foreshocks. *Nature*, *262*(5570), 677–679.  
613 <https://doi.org/10.1038/262677a0>
- 614 Kato, A., & Nakagawa, S. (2014). Multiple slow-slip events during a foreshock sequence of the  
615 2014 Iquique, Chile Mw 8.1 earthquake Aitaro. *Geophysical Research Letters*, *41*(15),

- 616 5420–5427. <https://doi.org/10.1002/2014GL061138>
- 617 Kilb, D., Gomberg, J., & Bodin, P. (2000). Triggering of earthquake aftershocks by dynamic  
618 stresses. *Nature*, *408*(6812), 570–574. <https://doi.org/10.1038/35046046>
- 619 King, G. C. P., Stein, R. S., & Lin, J. (1994). *Static Stress Changes and the Triggering of*  
620 *Earthquakes. Bulletin of the Seismological Society of America* (Vol. 84). Retrieved from  
621 <http://pubs.geoscienceworld.org/ssa/bssa/article-pdf/84/3/935/5341861/bssa0840030935.pdf>
- 622 Kuang, W., Yuan, C., & Zhang, J. (2021). Real-time determination of earthquake focal  
623 mechanism via deep learning. *Nature Communications*, *12*(1).  
624 <https://doi.org/10.1038/s41467-021-21670-x>
- 625 Lei, X., Huang, D., Su, J., Jiang, G., Wang, X., Wang, H., et al. (2017). Fault reactivation and  
626 earthquakes with magnitudes of up to  $M_w$  4.7 induced by shale-gas hydraulic fracturing in  
627 Sichuan Basin, China. *Scientific Reports*, *7*(1), 1–12. [https://doi.org/10.1038/s41598-017-](https://doi.org/10.1038/s41598-017-08557-y)  
628 [08557-y](https://doi.org/10.1038/s41598-017-08557-y)
- 629 Lei, X., Wang, Z., & Su, J. (2019a). Possible link between long-term and short-term water  
630 injections and earthquakes in salt mine and shale gas site in Changning, south Sichuan  
631 Basin, China. *Earth and Planetary Physics*, *3*(6), 510–525.  
632 <https://doi.org/10.26464/epp2019052>
- 633 Lei, X., Wang, Z., & Su, J. (2019b). The December 2018  $M_L$  5.7 and January 2019  $M_L$  5.3  
634 earthquakes in South Sichuan basin induced by shale gas hydraulic fracturing.  
635 *Seismological Research Letters*, *90*(3), 1099–1110. <https://doi.org/10.1785/0220190029>
- 636 Liu, J., & Zahradník, J. (2020). The 2019  $M_w$  5.7 Changning Earthquake, Sichuan Basin, China:  
637 A Shallow Doublet With Different Faulting Styles. *Geophysical Research Letters*, *47*(4), 1–  
638 9. <https://doi.org/10.1029/2019GL085408>

- 639 Meng, L., McGarr, A., Zhou, L., & Zang, Y. (2019). An investigation of seismicity induced by  
640 hydraulic fracturing in the Sichuan Basin of China based on data from a temporary seismic  
641 network. *Bulletin of the Seismological Society of America*, *109*(1), 348–357.  
642 <https://doi.org/10.1785/0120180310>
- 643 Peng, Z., & Zhao, P. (2009). Migration of early aftershocks following the 2004 Parkfield  
644 earthquake. *Nature Geoscience*, *2*(12), 877–881. <https://doi.org/10.1038/ngeo697>
- 645 Prejean, S. G., Hill, D. P., Brodsky, E. E., Hough, S. E., Johnston, M. J. S., Malone, S. D., et al.  
646 (2004). Remotely triggered seismicity on the United States west coast following the  $M_w$  7.9  
647 Denali fault earthquake. *Bulletin of the Seismological Society of America*, *94*(6 SUPPL. B),  
648 348–359. <https://doi.org/10.1785/0120040610>
- 649 Schultz, R., Skoumal, R. J., Brudzinski, M. R., Eaton, D., Baptie, B., & Ellsworth, W. (2020).  
650 Hydraulic fracturing-induced seismicity. *Reviews of Geophysics*, *58*(3), 1–43.  
651 <https://doi.org/10.1029/2019RG000695>
- 652 Shelly, D. R., Hill, D. P., Massin, F., Farrell, J., Smith, R. B., & Taira, T. (2013). A fluid-driven  
653 earthquake swarm on the margin of the Yellowstone caldera. *Journal of Geophysical*  
654 *Research E: Planets*, *118*(9), 4872–4886. <https://doi.org/10.1002/jgrb.50362>
- 655 Sheng, M., Chu, R., Ni, S., Wang, Y., Jiang, L., & Yang, H. (2020). Source Parameters of Three  
656 Moderate Size Earthquakes in Weiyuan, China, and Their Relations to Shale Gas Hydraulic  
657 Fracturing. *Journal of Geophysical Research: Solid Earth*, *125*(10), 1–14.  
658 <https://doi.org/10.1029/2020JB019932>
- 659 Sheng, M., Chu, R., Peng, Z., & Wei, Z. (2022). Earthquakes Triggered by Fluid Diffusion and  
660 Boosted by Fault Reactivation in Weiyuan , China Due to Hydraulic Fracturing *Journal of*  
661 *Geophysical Research : Solid Earth*, 1–18. <https://doi.org/10.1029/2021JB022963>

- 662 Tan, Y., Hu, J., Zhang, H., Chen, Y., Qian, J., Wang, Q., et al. (2020). Hydraulic Fracturing  
663 Induced Seismicity in the Southern Sichuan Basin Due to Fluid Diffusion Inferred From  
664 Seismic and Injection Data Analysis. *Geophysical Research Letters*, *47*(4), 1–10.  
665 <https://doi.org/10.1029/2019GL084885>
- 666 Waldhauser, F., & Ellsworth, W. L. (2000). A Double-difference Earthquake location algorithm:  
667 Method and application to the Northern Hayward Fault, California. *Bulletin of the*  
668 *Seismological Society of America*, *90*(6), 1353–1368. <https://doi.org/10.1785/0120000006>
- 669 Wang, M., Yang, H., Fang, L., Han, L., Jia, D., Jiang, D., & Yan, B. (2020). Shallow faults  
670 reactivated by hydraulic fracturing: The 2019 Weiyuan Earthquake Sequences in Sichuan,  
671 China. *Seismological Research Letters*, *91*(6), 3171–3181.  
672 <https://doi.org/10.1785/0220200174>
- 673 Wong, W. C. J., Zi, J., Yang, H., & JinRong Su, A. (2021). Spatial-temporal Evolution of  
674 Injection Induced Earthquakes in Weiyuan Area by Machine-Learning Phase Picker and  
675 Waveform Cross-correlation. *Earth and Planetary Physics*, *5*(0), 0–0.  
676 <https://doi.org/10.26464/epp2021055>
- 677 Yang, H., Zhou, P., Fang, N., Zhu, G., Xu, W., Su, J., et al. (2020). A shallow shock: The 25  
678 February 2019  $M_L$  4.9 Earthquake in the Weiyuan Shale Gas Field in Sichuan, China.  
679 *Seismological Research Letters*, *91*(6), 3182–3194. <https://doi.org/10.1785/0220200202>
- 680 Yao, D., Huang, Y., Peng, Z., & Castro, R. R. (2020). Detailed Investigation of the Foreshock  
681 Sequence of the 2010  $M_w$  7.2 El Mayor-Cucapah Earthquake. *Journal of Geophysical*  
682 *Research: Solid Earth*, *125*(6). <https://doi.org/10.1029/2019JB019076>
- 683 Yun, N., Zhou, S., Yang, H., Yue, H., & Zhao, L. (2019). Automated Detection of Dynamic  
684 Earthquake Triggering by the High-Frequency Power Integral Ratio. *Geophysical Research*

- 685        *Letters*, 46(22), 12977–12985. <https://doi.org/10.1029/2019GL083913>
- 686 Zhang, H., & Thurber, C. H. (2003). Double-difference tomography: The method and its  
687 application to the Hayward Fault, California. *Bulletin of the Seismological Society of*  
688 *America*, 93(5), 1875–1889. <https://doi.org/10.1785/0120020190>
- 689 Zhang, X., Zhang, J., Yuan, C., Liu, S., Chen, Z., & Li, W. (2020). Locating induced earthquakes  
690 with a network of seismic stations in Oklahoma via a deep learning method. *Scientific*  
691 *Reports*, 10(1), 1–12. <https://doi.org/10.1038/s41598-020-58908-5>
- 692 Zhang, Y., Y. An, F. Long, G. Zhu, M. Qin, Y. Zhong, Q. Xu, and H. Yang (2022), Short-term  
693 foreshock and aftershock patterns of the 2021 *Ms* 6.4 Yangbi earthquake sequence,  
694 *Seismological Research Letters*, doi:10.1785/0220210154.
- 695 Zhou, P. C., Ellsworth, W. L., Yang, H. F., Tan, Y. J., Beroza, G. C., Sheng, M. H., & Chu, R. S.  
696 (2021). Machine-learning-facilitated earthquake and anthropogenic source detections near  
697 the Weiyuan Shale Gas Blocks, Sichuan, China. *Earth and Planetary Physics*, 5(6), 532–  
698 546. <https://doi.org/10.26464/epp2021053>
- 699 Zhu, G., H. Yang, Y. Tan, M. Jin, X. Li, and W. Yang (2022) The cascading foreshock sequence  
700 of the *Ms* 6.4 Yangbi earthquake in Yunnan, China, *Earth and Planetary Sci. Lett.*,  
701 <https://doi.org/10.1016/j.epsl.2021.117594>
- 702 Zhu, W., & Beroza, G. C. (2019). PhaseNet: A deep-neural-network-based seismic arrival-time  
703 picking method. *Geophysical Journal International*, 216(1), 261–273.  
704 <https://doi.org/10.1093/gji/ggy423>
- 705 Zou, C., Ni, Y., Li, J., Kondash, A., Coyte, R., Lauer, N., et al. (2018). The water footprint of  
706 hydraulic fracturing in Sichuan Basin, China. *Science of the Total Environment*, 630, 349–  
707 356. <https://doi.org/10.1016/j.scitotenv.2018.02.219>
- 708